CrystEngComm

ROYAL SOCIETY OF CHEMISTRY

PAPER

View Article Online
View Journal | View Issue

Cite this: *CrystEngComm*, 2025, **27**, 1830

The role of aluminum doping in shaping the mechanical properties of p-type 4H-SiC†

Yanwei Yang,‡[ab] Zhouyu Tong, ‡[a] Xiaodong Pi, *[ab] Deren Yang [ab] and Yuanchao Huang *[ab]

Received 28th November 2024,
Accepted 21st February 2025

DOI: 10.1039/d4ce01196a

rsc.li/crystengcomm

In p-type 4H-SiC crystals, the doping of aluminum (Al) will affect mechanical properties due to changes in the crystal structure and defect dynamics. This study employs nanoindentation, Raman spectroscopy, and transmission electron microscopy (TEM) to investigate the effects of Al doping on the mechanical properties of p-type 4H-SiC. It compares samples with varying Al concentrations (undoped, low Al-doped, and high Al-doped) to examine changes in elastic modulus, hardness, and fracture toughness. Nanoindentation results reveal that Al doping reduces the hardness and fracture toughness of 4H-SiC, with the impact becoming more pronounced as the doping level increases. Microstructural analysis shows that Al doping facilitates dislocation formation and crack propagation, contributing to the observed mechanical degradation. Additionally, first-principles calculations provide insight into the underlying mechanisms, confirming that Al doping reduces the elastic modulus, hardness, and fracture toughness due to changes in shear modulus and bond strength. This work enhances the understanding of doping effects in p-type 4H-SiC and provides valuable information for the design and optimization of high-performance SiC wafers for industrial applications.

1. Introduction

With the advantages of wide band gap, high carrier mobility, and excellent thermal conductivity, 4H Silicon carbide (SiC) is considered as a leading next-generation semiconductor material for high-power electronics, microwave devices, and quantum information systems.[1–3] As a part of the silicon carbide family, p-type 4H-SiC has attracted great attention due to its low power consumption and fast switching ability in insulated gate bipolar transistor (IGBT) device fabrication.[4,5] Producing high-quality p-type 4H-SiC wafers is crucial for industrial applications, yet achieving defect-free wafers requires complex processing steps, including slicing, grinding, and polishing.[6–8] Due to its high brittleness and hardness, p-type 4H-SiC is prone to subsurface damage and crack propagation during diamond turning and slicing. Although subsequent grinding and chemical/mechanical polishing can gradually remove these defects, the low material removal rate makes the process time-consuming. Therefore, a deep understanding of p-type 4H-SiC's mechanical properties is essential to improving its fabrication, processing, and application.

Nanoindentation is a highly effective technique for probing the mechanical properties of materials at micro and nano scale.[9–11] Because the indenter can be used to simulate cutting tool tips or abrasive particles in mechanical machining, some researches had been carried it out on 4H-SiC. For instance, Liu *et al.* tested the hardness of the semi-insulating 4H-SiC by nanoindentation technology, yielding values of 34.8 GPa.[12] Goel *et al.* used a blunt Berkovich indenter to perform quasi-static nanoindentation on 4H-SiC and reported that elastic-to-plastic transition occurred when the shear stress was over 21 GPa.[13] Researchers have observed that the mechanical properties of 4H-SiC are primarily influenced by two factors: crystallographic orientation and dopant type.[14–18] For instance, Cody Kunka *et al.* concluded that the fracture toughness for [1 1 $\bar{2}$ 0] direction is 30% lower than that of [1 0 $\bar{1}$ 0] direction on the basal plane of 4H-SiC.[15] K. E. Prasad *et al.* also used nanoindentation technology to find a significant anisotropy in the hardness of 4H-SiC between different planes.[16] The second key factor is the type of dopant. In semi-insulating 4H-SiC, vanadium (V) doping is thought to inhibit the

[a] *State Key Laboratory of Silicon and Advanced Semiconductor Materials & School of Materials Science and Engineering, Zhejiang University, Hangzhou, Zhejiang 310027, China. E-mail: huangyuanchao@zju.edu.cn*
[b] *Institute of Advanced Semiconductors & Zhejiang Provincial Key Laboratory of Power Semiconductor Materials and Devices, ZJU-Hangzhou Global Scientific and Technological Innovation Center, Zhejiang University, Hangzhou, Zhejiang 311215, China*

† Electronic supplementary information (ESI) available: Please see the ESI for details about the definition of indenter angle, the phase transition and the Mulliken population of bond. See DOI: https://doi.org/10.1039/d4ce01196a

‡ Yanwei Yang and Zhouyu Tong contributed equally to this work.

formation and slip of dislocations, thereby enhancing the hardness and elastic modulus.[17] Conversely, for n-type 4H-SiC, nitrogen (N) doping promotes dislocation formation and weakens the covalent bonding, leading to a lower hardness and elastic modulus.[17,18] However, despite aluminum (Al) being the most common dopant in p-type 4H-SiC, its impact on the mechanical properties remains uninvestigated. This knowledge gap has hindered advancements in p-type 4H-SiC wafer technology.

In this study, nanoindentation technology is used to examine the impact of Al doping on the mechanical properties of p-type 4H-SiC, focusing on elastic modulus, hardness, and fracture toughness. Raman spectroscopy and transmission electron microscopy provide comparative microstructural analysis of different 4H-SiC wafers during nanoindentation. Finally, first-principles calculations reveal the mechanisms behind these changes in mechanical properties, contributing to a deeper understanding of doping effects in 4H-SiC and paving the way for the design of p-type 4H-SiC wafers with varied doping levels.

2. Methods

2.1 Materials and experiments

Three different Al doping concentrations of 4H-SiC are prepared: undoped, low Al-doped and high Al-doped. The concentrations of Al are found to be on the order of magnitude of 5×10^{18} cm^{-3} and 1×10^{20} cm^{-3}, for low and high doping levels, respectively. The undoped and Al-doped 4H-SiC crystals are purchased from Hangzhou Qianjing Semiconductor Co., Ltd. The thicknesses of the wafers are 350 μm. The Si-faces of all three wafers are treated with chemical–mechanical polishing to achieve a surface roughness below 0.2 nm. Nanoindentation tests are carried out using a nanoindentation system (Nanointender, USA) with a Berkovich indenter. The indenter orientation angle θ is defined as the angle between the indenter ridge and the wafer orientation flat ([1 1 $\bar{2}$ 0] direction), as shown in Fig. S1.† In order to reduce the effect of crystal orientation on the mechanical properties of 4H-SiC, all the tests are measured when θ is 30°.[19] Various peak loads ranging from 100 mN to 500 mN are carried out, with loading/unloading time of 10 s and holding time of 5 s.[9] Before each test, the system is calibrated using a standard fused-silica specimen. The loading/unloading cycles are repeated for six times to obtain reliable data. The cross-sectional transmission electron microscopy (TEM) specimens were processed using a focused ion beam (FIB, Helios 5 UX). TEM and high-resolution TEM (HRTEM) images are obtained by a FEI Tecnai G2 TEM at an accelerating voltage of 300 kV.

2.2 First-principles calculations

First-principles calculations are carried out by the projector-augmented wave (PAW) method, as implemented in the Vienna *ab initio* simulation package (VASP). The wave functions are expanded by using the plane waves up to a kinetic energy cutoff of 500 eV. The Perdew–Burke–Ernzerhof revised for solids (PBEsol) functional with the GGA exchange correlation is adopted. The models consist of a supercell with 128 atoms for undoped 4H-SiC and 127 atoms with one Al atom for p-type 4H-SiC. Supercell size and atomic positions are fully relaxed until the total energy per cell and the force on each atom converge to less than 1×10^{-6} eV and 0.01 eV/ Å, respectively. For Brillouin zone integration, the Monkhorst–Pack scheme with a Γ-centered 2 × 2 × 2 special *k*-points mesh is used.[20]

3. Results and discussion

3.1 Load–displacement characteristics

The load–displacement curves of three types 4H-SiC—undoped, low Al-doped, and high Al-doped—are smooth in the range from 100 to 500 mN, as shown in Fig. 1a–c. A pop-in event, associated with structural changes such as dislocation formation, crack propagation, phase transformation, and defect nucleation, occurs once the load reaches 300 mN.[14,21,22] The pop-in platforms in the plot under large loads is mainly because of the formation and propagation of cracks.[12] Under the largest peak load of 500 mN, it can be observed that the maximum indentation depth for undoped 4H-SiC, low Al-doped and high Al-doped p-type 4H-SiC is 1188 nm, 1402 nm, and 1431 nm, respectively. Among these three types of curves, the slope of the load–displacement curve decreases as Al content in the wafers increases. This phenomenon implies that the doping of Al makes 4H-SiC hardness reduced, and this trend becomes more obvious with the increase of Al content.

The elastic modulus and hardness measured by nanoindentation are shown in Fig. 2a and b. Both initially decrease with increasing load before stabilizing, partly due to the indenter size effect.[23] The elastic modulus, which indicates the stiffness, is significantly higher in undoped 4H-SiC compared to p-type 4H-SiC, with values of 465 GPa, 434 GPa, and 418 GPa for undoped, low, and high Al-doped samples, respectively. Compared to V-doped 4H-SiC reported in the literature, the Al-doped samples exhibit a lower elastic modulus.[12] Similarly, the hardness of undoped 4H-SiC (34.0 GPa) is higher than that of p-type 4H-SiC, decreasing as Al concentration increases: approximately 31.2 GPa at 5×10^{18} cm^{-3} and 28.7 GPa at 1×10^{20} cm^{-3}, indicating that p-type 4H-SiC becomes "softer" with Al doping.

Fig. 3 shows the morphology of the sample after nanoindentation with a 500 mN applied force. The crack length varies in different samples, increasing with higher Al doping content. This indicates a gradual weakening of the material's strength as the Al concentration rises. Under the identical stress condition, the longer the crack length, the lower the hardness. Moreover, the crack length is closely linked to the fracture toughness of the material. The indentation fraction toughness (K_{IC}) is calculated by:[12]

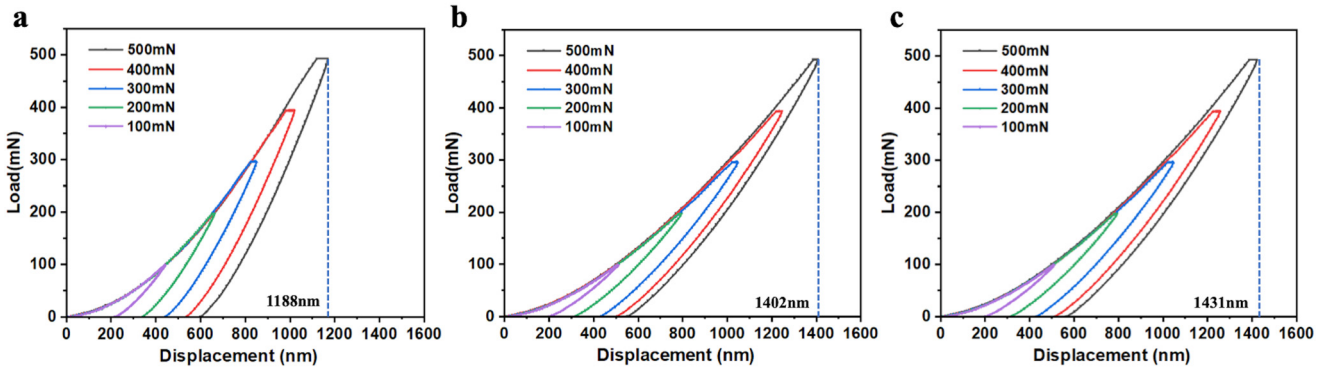

Fig. 1 (a–c) Load–displacement curves for the a) undoped, b) low Al-doped p-type 4H-SiC, and c) high Al-doped p-type 4H-SiC.

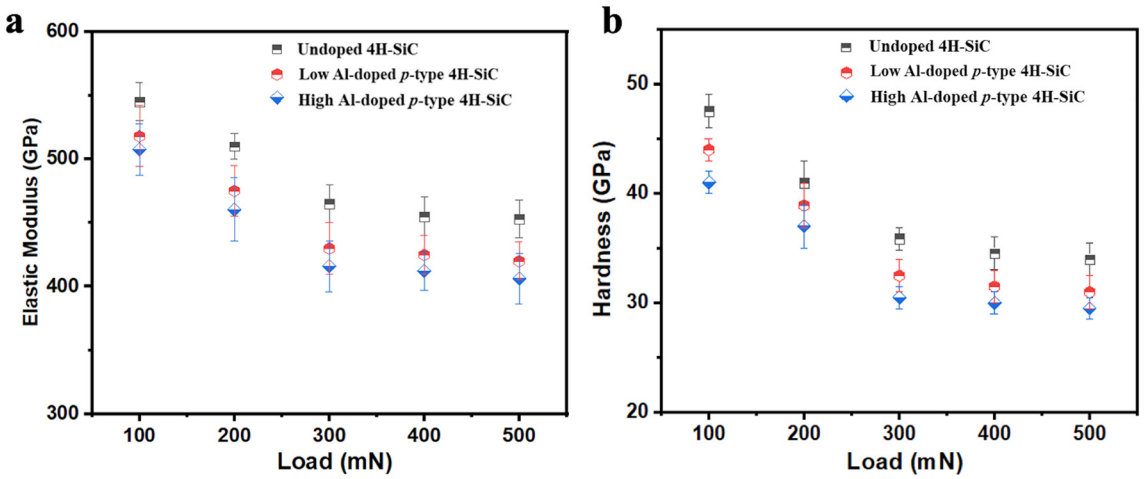

Fig. 2 The average values of elastic modulus and hardness as functions of the load for undoped 4H-SiC, low Al-doped p-type 4H-SiC and high Al-doped p-type 4H-SiC: a) elastic modulus, b) hardness.

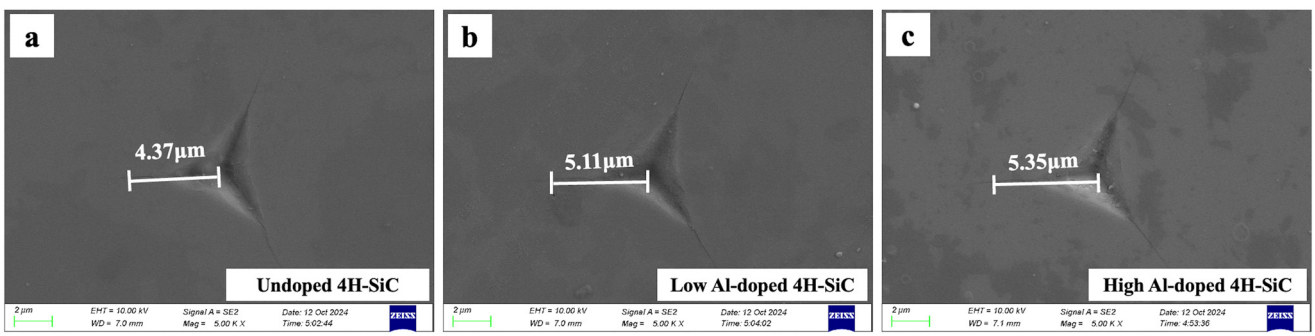

Fig. 3 SEM images of an indent imprint in a) undoped 4H-SiC, b) low Al-doped p-type 4H-SiC, c) high Al-doped p-type 4H-SiC.

$$K_{IC} = 0.016\left(\frac{a}{l}\right)^{\frac{1}{2}}\left(\frac{E}{H}\right)^{\frac{2}{3}}\frac{P}{c^{2/3}} \quad (1)$$

where a is the indent length from center to corner, l is the crack length from the indent corner to the crack tip, P is the applied load, E and H are the elastic modulus and hardness, and c is the average distance from the center of the indenter to the edge of the crack. According to this formula, a longer crack results in a smaller fracture toughness value, explaining the observed trend in fracture toughness. As Al doping increases, the fracture toughness decreases in the order of undoped 4H-SiC, low Al-doped p-type 4H-SiC, and high Al-doped p-type 4H-SiC. The fracture toughness (K_{IC}) values for the three types of wafers are 2.53 ± 0.02 MPa $m^{1/2}$, 1.86 ± 0.02 MPa $m^{1/2}$, and 1.76 ± 0.02 MPa $m^{1/2}$, respectively. This confirms that Al doping reduces the fracture toughness of 4H-SiC, with the effect becoming more pronounced as the Al content increases.

3.2 Phase transformation

The impact of Al doping on the microstructure of 4H-SiC after indentation is also examined using micro-Raman spectroscopy. As shown in Fig. 4, all the spectra show the typical crystal peaks at 776 cm^{-1} and 796 cm^{-1}, corresponding to the folded transverse optical (TO) modes of 4H-SiC.[24] Although differences in peak intensity are observed, no new peaks emerge, consistent with previous reports.[19] Obviously, the peak near 796 cm^{-1} shows little change in intensity, while the peak near 776 cm^{-1} weakens significantly after indentation. For example, in the case of low Al-doped p-type 4H-SiC, the pristine wafer has characteristic peak intensities of 3556 and 125 at 776 cm^{-1} and 796 cm^{-1}, respectively. After indentation, the intensities of these peaks drop to 988 and 107. Specifically, the intensity at 776 cm^{-1} decreases by approximately three times, while the intensity at 796 cm^{-1} only decreases by about half. This change is quantified by the ratio r (TO-776/TO-796), which is lower in the indented sample compared to the pristine one. Nakashima *et al.* reported that 3C-SiC has only one peak near 776 cm^{-1}, while 4H-SiC has two characteristic peaks on TO mode located at 776 cm^{-1} and 796 cm^{-1}, with the 776 cm^{-1} peak being much stronger.[24] The fact that the peak at 796 cm^{-1} does not decrease as sharply suggests the presence of 3C-SiC, indicating a phase transformation from 4H-SiC to 3C-SiC. This observation is consistent with the findings of Matsumoto *et al.*, who reported a phase transformation from 4H-SiC to 3C-SiC during nanoindentation in the analysis of the damage regions.[19] The lower strength and elastic modulus of p-type 4H-SiC make it more prone to deformation, which facilitates the transformation from 4H-SiC to 3C-SiC. Moreover, taking low Al-doped p-type 4H-SiC as an example, Fig. S2† reveal that p-type 4H-SiC undergoes a phase transition during the nanoindentation process. The ABAC stacking sequence of 4H-SiC is clearly. Under the action of force, an atomic arrangement corresponding to the ABC stacking order of 3C-SiC emerges, which also confirms the results observed in the Raman analysis. The fast Fourier transform (FFT) diffraction peaks shown in Fig. S2b† illustrates a typical diffraction pattern of 4H-SiC. In addition, the FFT peaks provide direct evidence that the crystal structure aligns with the <110> direction of 3C-SiC.[12] Fig. S3† shows the underlying mechanism for the phase transformation after nano identification. The atoms in 4H-SiC would change their stacking positions by the slip in 1/3 [1 $\bar{1}$ 0 0] direction on the (0 0 0 1) plane, *i.e.* A → C, C → B, B → A. Thus, 3C-SiC structure would be formed by the repeated change of atom sites under the indentation stress.

3.3 Microstructure observation

To further explore the changes of subsurface microstructure induced by nanoindentation, TEM samples are extracted from the residual indents generated under 500 mN with orientation angles 30°. Fig. 5a–c shows the locations of nanoindents on p-type 4H-SiC with different doping levels, which are prepared and sampled using a focused ion beam (FIB). Various types of dislocations are observed beneath the nanoindentation sites. In undoped 4H-SiC, dislocation density is low, with dislocations mainly along the basal plane and threading directions, resulting in fewer dislocations and shorter cracks due to high hardness and elastic modulus. In low-Al-doped 4H-SiC, dislocation density increases as Al doping, leading to more dislocations, longer cracks, and lower fracture toughness. In high-Al-doped 4H-SiC, dislocation density is the highest, with extensive subsurface damage and further decreases in hardness and fracture toughness. TEM images confirm that dislocation density rises with Al doping, correlating with weakened crystal structure and progressive mechanical property degradation. Fig. 5d–f display the enlarged pattern corresponding to the red box, revealing that basal plane dislocations are mainly distributed along the direction [1 1 $\bar{2}$ 0], while threading edge dislocations are primarily oriented along the direction [0 0 0 $\bar{1}$] direction. Similar dislocations are previously reported for 4H- and 6H-SiC because of the slip systems in crystal SiC, *i.e.* (0 0 0 1) [1 $\bar{2}$ 1 0] or (0 0 0 1) [0 1 $\bar{1}$ 0].[14,19] The formation of these dislocations facilitates the release of the stress within the crystal during the

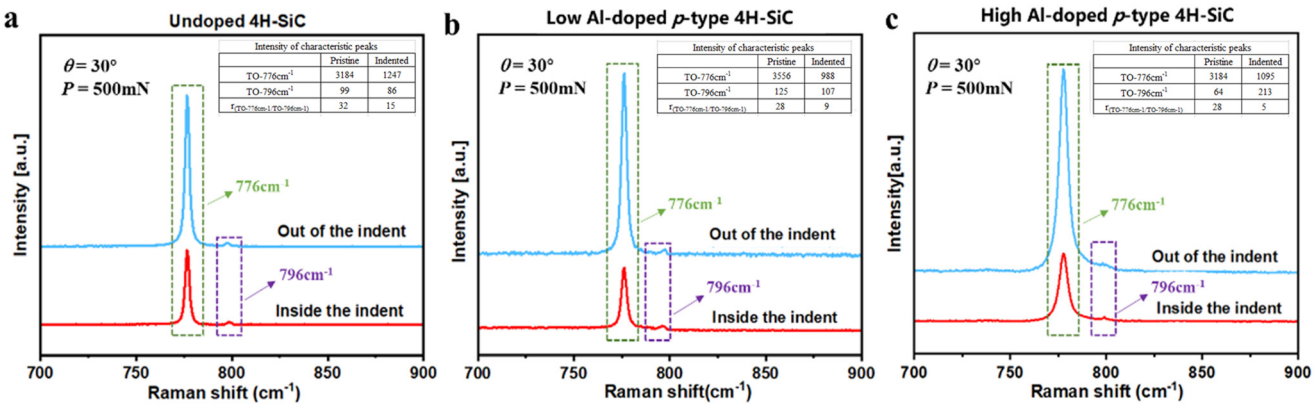

Fig. 4 Raman spectra obtained at the pristine surface and nanoindented surface for (a) undoped, (b) low Al-doped p-type 4H-SiC, and (c) high Al-doped p-type 4H-SiC under the peak load of 500mN. The inset table summarizes the intensity of characteristic peak.

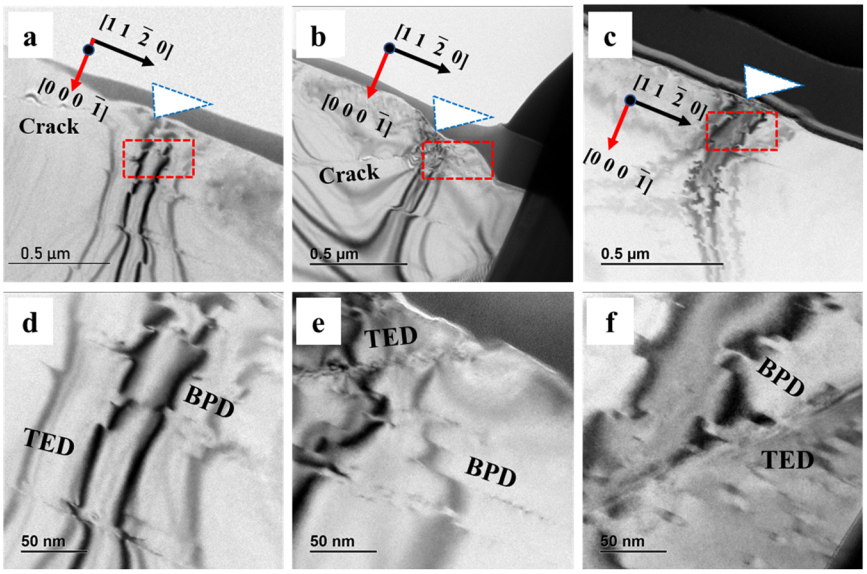

Fig. 5 (a–c) Cross-sectional transmission electron microscopy (TEM) image of an indent imprint in (a and d) undoped 4H-SiC, (b and e) low Al-doped p-type 4H-SiC, and (c and f) high Al-doped p-type 4H-SiC. (d–f) Zoom-in images for the red regions.

nanoindentation process. The uneven distribution of stress is the primarily factor driving dislocation nucleation in 4H-SiC.[25] During nanoindentation, the crystal primarily experiences compressive and shear forces. The compressive force induces cracks, defects, and deformations, whereas the shear force leads to the formation of dislocations within the crystal lattice. It is worth noting that the direction of basal plane dislocations is mainly preferentially distributed along the direction [1 1 $\bar{2}$ 0], which is consistent with the results reported in the literature.[26]

3.4 Mechanism

From the above conclusion, the elastic modulus, the hardness, and the fracture roughness of 4H-SiC decrease progressively in the order of undoped, low Al-doped, and high Al-doped. To explore the underlying mechanisms for these changes, theoretical values are derived using first-principles calculations for undoped 4H-SiC and p-type 4H-SiC, and the results are summarized. As shown in Table 1, the elastic modulus calculated from first-principles decreases from 446.1 GPa to 403.5 GPa after Al doping. The bulk modulus remains largely unchanged at approximately 223.0 GPa, while the shear modulus decreases from 191.1 GPa to 168.3 GPa. For the shear modulus, it is the ability of the material to resist shear strain and the large modulus indicates the strong rigidity. The shear modulus of 4H-SiC is higher than that of p-type 4H-SiC, indicating that p-type 4H-SiC has lower strength.

The theoretical hardness of covalent crystals is calculated as:[30]

$$H_T = 2((G/B)^2 G)^{0.585} - 3 \quad (2)$$

where H_T represented the theoretical hardness, G and B are shear and bulk modulus (MPa), respectively. Following Al doping, the calculated hardness decreases from 32.9 GPa to 25.8 GPa. According to eqn (2), hardness is directly proportional to G and inversely proportional to B. Therefore, the primary reason for the hardness reduction can be attributed to the decrease in G.

The theoretical K_{IC} of 4H-SiC is calculated as:[31]

$$K_{IC} = V_0^{1/6} \cdot G \cdot (B/G)^{1/2} \quad (3)$$

where V_O represented the volume per atom (m^3), the unit of K_{IC} is MPa $m^{1/2}$. According to eqn (3), K_{IC} is directly proportional to both G and B. Therefore, the decrease in G due to Al doping also contributes to a reduction in K_{IC}.

Table 1 Theoretical values calculated from first principles

	Undoped 4H-SiC		P-type 4H-SiC		
	Theoretical value	Experimental value	Theoretical value	Experimental value	Reference
Bulk modulus (GPa)	223.6	—	223.1	—	—
Shear modulus (GPa)	191.1	—	168.3	—	—
Elastic modulus (GPa)	446.1	465.0, 461.3, 468.4, 423.0	403.5	418.0	11, 14, 27, 28
Hardness (GPa)	32.9	34.5, 35.8, 36.8, 36.0	25.8	28.7	14, 19, 27, 28
K_{IC} (Mpa $m^{1/2}$)	3.05	2.55, 3.42, 2.10, 1.80	2.86	1.76	11, 23, 27, 29

The elastic modulus is intrinsically related to bond strength, as reported in numerous studies, including Wang *et al.*, who proposed a theoretical model linking bond type and stiffness to elastic properties.[32] For 4H-SiC, bond strength is similarly important. The Mulliken population analysis in Fig. S4† shows that bond strength near Al atoms decreases, with the Al–C bond population at 0.63, while the Si–C bond near the Al atom is 0.77, and the Si–C bond in unaffected regions is 0.78. Thus, Al doping causes not only a reduction in bond population in Al–C bonds but also affects neighboring Al–Si bond strength, resulting in a lower elastic modulus for p-type 4H-SiC.[33] Besides, the reduced hardness of p-type 4H-SiC compared to undoped 4H-SiC can be attributed to the interactions of dislocations in the plastic zone under indentation and the effect of surrounding elastic materials on plastic deformation. Studies by scientists indicate that stacking fault energy (SFE) is crucial in determining elastic properties, with undoped 4H-SiC showing higher SFE than p-type 4H-SiC.[34–36] Lower SFEs facilitate a higher density of dislocations in p-type 4H-SiC, as seen in Fig. 5, where p-type 4H-SiC exhibits greater dislocation density under the same indentation process, further contributing to its lower hardness. Moreover, the fracture toughness of 4H-SiC also decreases with Al doping, as predicted by theoretical models. The K_{IC} of a crystal is influenced by the bond strength and the resistance to crack propagation within the structure. The lower bond strength in p-type 4H-SiC contributes to reduced resistance to crack propagation, in line with experimental observations.

Although Al doping in SiC has a saturation limit and can degrade mechanical properties, alternative strategies like co-doping with elements such as boron (B) or nitrogen (N) can be used to improve mechanical properties.[12,37] Techniques such as irradiation or ion implantation can be used to modify the microstructure and improve mechanical properties. For instance, irradiation technology can reduce dislocation density and improve crystal quality, while ion implantation can introduce compressive stresses that enhance hardness.[38]

4. Conclusion

In this study, the impact of Al doping on the mechanical properties and microstructure of p-type 4H-SiC is systematically investigated using nanoindentation, Raman spectroscopy, TEM, and first-principles calculations. Nanoindentation tests show that the hardness and elastic modulus of p-type 4H-SiC decrease with higher Al doping, and the material becomes more prone to deformation, as evidenced by larger indentation depths, and longer crack lengths. Additionally, Raman spectroscopy reveals a phase transformation appears from 4H-SiC to 3C-SiC during nanoindentation, which is more pronounced in Al-doped samples. TEM analysis further confirms the formation of various dislocations and subsurface damage, with an increase in dislocation density as the Al content increases. The first-principles calculations support these findings by demonstrating a reduction in bond strength in Al-doped p-type 4H-SiC compared to undoped 4H-SiC. These insights provide valuable information on the deformation mechanisms and structural integrity of p-type 4H-SiC, which are crucial for optimizing the processing and application of this material in semiconductor devices.

Data availability

The data that support the findings of this study are available at zenodo at **https://doi.org/10.5281/zenodo.14233352**.

Author contributions

Yanwei Yang: conceptualization, methodology, investigation, formal analysis, data curation, writing – original draft, validation; Zhouyu Tong: data curation, validation, investigation; Xiaodong Pi: funding acquisition, supervision, resources; Deren Yang: writing – review & editing, funding acquisition, supervision, project administration. Yuanchao Huang: funding acquisition, supervision, resources. Yanwei Yang and Zhouyu Tong contributed equally to this work.

Conflicts of interest

The authors have no conflicts to disclose.

Acknowledgements

This study is mainly supported by the "Pioneer" and "Leading Goose" R&D Program of Zhejiang Province (Grant No. 2022C01021 & 2023C01010) and Natural Science Foundation of Zhejiang Province (LQ24F040001). Partial support is provided by the Natural Science Foundation of China for Innovative Research Groups (Grant No. 61721005) and the Fundamental Research Funds for the Central Universities (226-2022-00200).

References

1 R. Wang, Y. Huang, D. Yang and X. Pi, *Appl. Phys. Lett.*, 2023, **122**, 180501.
2 M. Cabello, V. Soler, G. Rius, J. Montserrat, J. Rebollo and P. Godignon, *Mater. Sci. Semicond. Process.*, 2018, **78**, 22–31.
3 Y. W. Yang, Z. Y. Tong, X. D. Pi, D. R. Yang and Y. C. Huang, *Phys. Scr.*, 2024, **99**(9), 092001.
4 Y. C. Huang, R. Wang, Y. Q. Zhang, D. R. Yang and X. D. Pi, *J. Appl. Phys.*, 2022, **131**(18), 185703.
5 G. B. Wang, D. Sheng, Y. F. Yang, Z. S. Zhang, W. J. Wang and H. Li, *Cryst. Growth Des.*, 2024, **24**(13), 5686–5692.
6 Y. Q. Zhou, Y. H. Huang, J. M. Li, W. S. Lv and F. L. Zhu, *Diamond Relat. Mater.*, 2023, **133**, 109710.
7 Y. Zhang, H. Y. N. Chen, D. Z. Liu and H. Deng, *Appl. Surf. Sci.*, 2020, **525**, 146532.
8 E. Kim, Y. Shimotsuma, M. Sakakura and K. Miura, *Opt. Mater. Express*, 2017, **7**(7), 2450–2460.

9 X. S. Liu, R. Wang, J. R. Zhang, Y. H. Lu, Y. Q. Zhang, D. R. Yang and X. D. Pi, *J. Phys. D: Appl. Phys.*, 2022, **55**(49), 494001.
10 A. Sciuto, P. P. Barbarino, D. Mello and G. D'Arrigo, *Mater. Des.*, 2024, **239**, 112751.
11 S. H. Shi, Y. Q. Yu, N. C. Wang, Y. Zhang, W. B. Shi, X. J. Liao and N. Duan, *Materials*, 2022, **15**(7), 2496.
12 X. S. Liu, J. R. Zhang, B. J. Xu, Y. H. Lu, Y. Q. Zhang, R. Wang, D. R. Yang and X. D. Pi, *Appl. Phys. Lett.*, 2022, **120**(5), 052105.
13 S. Goel, J. W. Yan, X. C. Luo and A. Agrawal, *J. Mech. Behav. Biomed. Mater*, 2014, **34**, 330–337.
14 A. Nawaz, W. G. Mao, C. Lu and Y. G. Shen, *J. Mech. Behav. Biomed. Mater*, 2017, **66**, 172–180.
15 C. Kunka, A. Trachet and G. Subhash, *J. Am. Ceram. Soc.*, 2015, **98**(6), 1891–1897.
16 K. E. Prasad and K. T. Ramesh, *J. Alloys Compd.*, 2019, **770**, 158–165.
17 X. S. Liu, R. Wang, J. R. Zhang, Y. H. Lu, Y. Q. Zhang, D. R. Yang and X. D. Pi, *J. Phys. D: Appl. Phys.*, 2022, **55**(33), 334002.
18 J. J. Li, H. Luo, G. Yang, Y. Q. Zhang, X. D. Pi, D. R. Yang and R. Wang, *Phys. Rev. Appl.*, 2022, **17**(5), 054011.
19 M. Matsumoto, H. Huang, H. Harada, K. Kakimoto and J. W. Yan, *J. Phys. D: Appl. Phys.*, 2017, **50**(26), 265303.
20 Y. C. Huang, Y. X. Qian, Y. Q. Zhang, D. R. Yang and X. D. Pi, *J. Appl. Phys.*, 2022, **132**(1), 015701.
21 R. Abram, D. Chrobak and R. Nowak, *Phys. Rev. Lett.*, 2017, **118**(9), 095502.
22 L. H. Xue, G. Feng, B. Gao and S. Liu, *J. Appl. Phys.*, 2023, **605**, 127082.
23 X. S. Rao, F. H. Zhang, X. C. Luo and F. Ding, *Mater. Sci. amp; Eng. A: Struct. Mater.: Prop. Microstruct. Process.*, 2019, **74**, 426–435.
24 S. Nakashima, M. Higashihira, K. Maeda and H. Tanaka, *J. Am. Ceram. Soc.*, 2003, **86**(5), 823–829.
25 N. D. Bassim, M. E. Twigg, M. A. Mastro, C. R. Eddy, T. J. Zega, R. L. Henry, J. C. Culbertson, R. T. Holm, P. Neudeck, J. A. Powell and A. J. Trunek, *J. Cryst. Growth*, 2007, **304**(1), 103–107.
26 J. Li, G. Yang, X. Liu, H. Luo, L. Xu, Y. Zhang, C. Cui, X. Pi, D. Yang and R. Wang, *J. Phys. D: Appl. Phys.*, 2022, **55**(46), 463001.
27 P. Chai, S. J. Li, Y. Li, L. Liang and X. C. Yin, *Micromachines*, 2020, **11**(1), 102.
28 H. X. Wang, Z. G. Dong, R. K. Kang and S. Gao, *Appl Surf Sci*, 2024, **665**, 160293.
29 D. Y. Hou, M. Liu, S. Liu and F. Q. Yang, *Int. J. Mech. Sci.*, 2024, **270**, 109096.
30 X. Q. Chen, H. Y. Niu, D. Z. Li and Y. Y. Li, *Intermetallics*, 2011, **19**(9), 1275–1281.
31 H. Y. Niu, S. W. Niu and A. R. Oganov, *J. Appl. Phys.*, 2019, **125**(6), 065105.
32 Y. X. Li, H. J. Xu, P. F. Shi, J. X. Xu and Y. Wang, *Ceram. Int.*, 2024, **50**(19), 36472–36478.
33 M. D. Segall, R. Shah, C. J. Pickard and M. C. Payne, *Phys. Rev. B: Condens. Matter Mater. Phys.*, 1996, **54**(23), 16317–16320.
34 H. Suo, T. Yamashita, K. Eto, A. Miyasaka, H. Osawa, T. Kato and H. Okumura, *Jpn. J. Appl. Phys.*, 2022, **61**(10), 105502.
35 H. Sakakima, S. Takamoto, A. Hatano and S. Izumi, *J. Appl. Phys.*, 2020, **127**(12), 125703.
36 K. Maeda, K. Murata, I. Kamata and H. Tsuchida, *Appl. Phys. Express*, 2021, **14**(4), 044001.
37 E. Kazuma, S. Hiromasa, K. Tomohisa and O. Hajime, *J. Cryst. Growth*, 2017, **470**, 154–158.
38 M. Bathen, A. Galeckas, J. Coutinho and L. Vines, *J. Appl. Phys.*, 2020, **127**, 085701.

